

Diurnal soil water dynamics in the shallow vadose zone (field site of China University of Geosciences, China)

Yijian Zeng · Li Wan · Zhongbo Su · Hirotaka Saito ·
Kangle Huang · Xusheng Wang

Received: 13 May 2008 / Accepted: 8 July 2008 / Published online: 31 July 2008
© Springer-Verlag 2008

Abstract Because of the relatively low soil moisture in arid or semi-arid regions, water vapour movement often predominates in the vadose zone and affects the partitioning of energy among various land surface fluxes. In an outdoor sand bunker experiment, the soil water content at 10 and 30 cm depth were measured at hourly intervals for 2.5 days during October 2004. It was found that the soil moisture reached the daily maximum value (5.9–6.1% at 10 cm and 11.9–13.1% at 30 cm) and minimum value (4.4–4.5% at 10 cm and 10.4–10.8% at 30 cm) at midday (0–1 p.m. for 10 cm and 2–3 p.m. for 30 cm) and before dawn (2–3 a.m. for 10 cm and 4–5 a.m. for 30 cm), respectively. The modified HYDRUS-1D code, which refers to the coupled water, water vapour and heat transport in soil, was used to simulate the moisture and water vapour flow in the soil. The numerical analyses provided insight into the diurnal movement of liquid water and water vapour driven by the gradients of pressure heads and temperatures in the subsurface zone. The simulated temperature and water content were in good agreement with the measured

values. The spatial–temporal distribution of liquid water flux, water vapour flux and soil temperature showed a detailed diurnal pattern of soil water dynamics in relatively coarse sand.

Keywords Vadose zone · Water vapour · Coupled heat and water movement model · Temperature gradient

Introduction

Soil moisture in the unsaturated zone near the soil surface plays a critical role in partitioning precipitation into surface runoff, evaporation, and groundwater recharge. Simultaneously, soil moisture affects the conversion of incoming solar and atmospheric radiation into sensible, latent, and radiant heat losses. Along with solar radiation and soil nutrients, the availability of soil moisture is the key to plant growth and production of crops. As such, soil moisture is not only important to agriculture but may also potentially affect the global climate and is therefore considered as a critical area for global climate change studies (Kerr et al. 2001; Entekhabi et al. 2004).

There are many existing land surface schemes, which provide boundary conditions for global climate models and numerical weather prediction models, estimating exchanges of the fluxes of energy, heat and water vapour between the land surface and the atmosphere (Dickinson et al. 2006). All these schemes are based on parameterizing plot scale sensible heat and moisture transfers in the soil–vegetation–atmosphere system and are scaled up to a model grid using a statistical approach. The treatment of soil moisture processes determines to a large extent the volume of the exchanges in these schemes, which consequently

Electronic supplementary material The online version of this article (doi:10.1007/s00254-008-1485-8) contains supplementary material, which is available to authorized users.

Y. Zeng (✉) · L. Wan · K. Huang · X. Wang
School of Water Resources and Environment,
China University of Geosciences, 100083 Beijing, China
e-mail: yijian@itc.nl

Y. Zeng · Z. Su
International Institute for Geo-information Science and Earth
Observation, 7500 AA Enschede, The Netherlands

H. Saito
Institute of Symbiotic Science and Technology, Tokyo
University of Agriculture & Technology,
Fuchu, Tokyo 183-8509, Japan

influences other variables in the atmosphere (e.g. clouds and precipitation). The importance of soil moisture has resulted in a very large number of models, which simulate water transport both in the liquid and vapour phase. Most of these models are based on theories that describe the coupled energy and mass flow in soil, considering the microscopic structure of a porous medium (Philip 1957; Philip and De Vries 1957; De Vries 1958; Milly and Eagleson 1980; Milly 1984b). There are also other models, which are based on the thermodynamics theory of irreversible process, adopted to analyse the transport of heat and mass (Taylor and Stewart 1960; Taylor and Cary 1964; Groenevelt and Kay 1974; Kay and Groenevelt 1974).

The soil moisture variation in arid and semi-arid regions is characterized by water vapour transport in the surface soil layer, since liquid water movement could be infinitesimal due to extremely dry soil conditions (Griffoll and Cohen 1999; Salzmann et al. 2000). This dominant water vapour transport can result in the conservation of liquid water in the unsaturated zone (Scanlon 1992; Scanlon and Milly 1994); subsequently, it plays an important role in maintaining vegetation and ecosystems in arid or semi-arid areas (Shiklomanov et al. 2004). Moreover, the way of accumulating liquid water from water vapour transport has been applied in order to produce fresh drinking water in dry areas by burying perforated pipes in the soil (Hausherr and Ruess 1993; Gustafsson and Lindblom 2001; Lindblom and Nordell 2006).

Due to the importance of soil moisture, many field or laboratory experiments were conducted in order to observe the changes in water content due to water vapour transport and subsequently to analyse the soil water dynamics that involve the movement of liquid water, water vapour and heat. In order to verify the numerical model for the coupled flow derived from the thermodynamic theory of irreversible process (Cary and Taylor 1962a, b), from 1962 to 1979, Cary and co-workers conducted a number of indoor experiments (Cary 1963, 1964, 1965, 1979). In the same period, Rose published a series of papers (Rose 1963a, b, 1968a, b, 1971) in order to test the theory of coupled transport in porous medium, which was developed by Philip and de Vries (1957). Except for the laboratory experiments, quantitative study of soil moisture transport in the field environment has been conducted by some other investigators, such as: Cary 1966; Jackson 1973 etc. After almost two decades of discussing the aforementioned experiments, the Philips and de Vries model (hereafter, referred to as the PDV model) remains as prominent as ever, even though the contemporary version has been slightly modified. (Milly 1982, 1984a, b; Braud et al. 1995; Shurbaji and Phillips 1995; Milly 1996; Nassar and Horton 1997).

The reason for the wide use of the PDV model is mainly due to the enhancement factor for water vapour transport. There are two postulated mechanisms for enhanced water vapour transfer (Philip and De Vries 1957): the first assumption is that the water vapour can flow through the liquid island between solid particles by condensing on one side of the liquid island and subsequently evaporating on the other side; the second postulate considers local temperature gradients in the air-filled pores, which might be significantly higher than the average temperature gradient. According to these assumptions, the humidity of the air adjacent to the water in soil pores, which is determined by the local equilibrium hypothesis, is often substituted for the land surface humidity. However, such substitution is invalid, except for the humid conditions below the evaporation front, which takes place near the surface when the evaporative demand is greater than the ability of the soil to conduct water in the liquid phase and a liquid–vapour phase discontinuity occurs (Asghar 1996; Rose et al. 2005). This invalidation triggers the studies on the changes in soil water content in the topsoil, which includes the parameterization of evaporation from the soil surface (Kondo and Okusa 1990; Kondo et al. 1992; Yamanaka and Yonetani 1999; Konukcu et al. 2004; Gowing et al. 2006) and the exploration of the mechanisms by which water is added to the surface soil layer (Jacobs and Heusinkveld 2000; Jacobs et al. 1999; Agam and Berliner 2006; Agam et al. 2004).

Although the theory of coupled water, water vapour and heat transport in soil is widely recognized and thus extensively tested and reinforced, very few studies have demonstrated and evaluated soil water dynamics in time and space, both simultaneously and continuously. The common approach to address this issue is either to analyse the profile soil water and temperature information at specific times (Zhang and Berndtsson 1991; Athavale et al. 1998; Mmolawa and Or 2003; Griffoll et al. 2005; Saito et al. 2006) or to assess the time-series information at specific depths (Kemp et al. 1997; Schelde et al. 1998; Starr and Paltineanu 1998; Wang 2002; Starr and Timlin 2004). In this study, observed soil water content and temperature were used in order to calibrate the performance of the modified HYDRUS-1D code in sand. Then, the modified HYDRUS-1D code was used to produce temporal and spatial information of the coupled water, water vapour and heat transport. The space–time information represents a two-dimensional field and a dependent specific flux (e.g. thermal water vapour flux) or temperature as a third dimension. The space–time information and dependent specific fluxes or temperatures (all of which contain discrete values) were used directly in an interpolation and smoothing procedure. This was done to create a continuous

three-dimensional field for the diurnal pattern interpretation of soil water dynamics.

Materials and methods

In situ setup

The experiment was conducted in an outdoor sand bunker in a field of the China University of Geosciences (Beijing) from 4 October to 7 October 2004. Although the field was surrounded by some trees, the study area was almost completely flat and completely exposed to sun light. Before and during the observation period, there was no precipitation, and the conditions in the field were reported as clear skies and light winds. Maximum and minimum air temperatures in this field ranged from 28.3 to 35°C (0–2 p.m.) and 10.8–12°C (5–7 a.m.), respectively; the maximum and minimum relative humidity ranged from 85.5 to 97.9% (4–7 a.m.) and 33.2–34% (0–3 p.m.), respectively. In addition, the atmospheric pressure and wind speed ranged from 1012.25 to 1017.54 hPa and from 0 to 1.45 m/s. The sand-filled bunker (1 m×1 m×1 m) was located in the centre of the field. The surrounding soil was paved with a poly-chlorothene film in order to avoid its influence on the distribution of soil water content.

During the observation, atmospheric pressure and solar radiation were measured at a fixed position close to the sand bunker—where the instruments could not influence the interactions between the atmosphere and the sand bunker. The atmospheric pressure was measured by the DYM4-1 aneroid barometer (Chan Chun Meteorological Instrument Factory, Inc., China), which has the accuracy of ± 1.2 hPa; while solar radiation was monitored by a Testo-545 pyranometer (Testo, Inc., Flanders, NJ), the accuracy of reading of which is: to DIN5032, part 6, $F1 = 8\%$, $F1 = V(\lambda)$ adaption, $F2 = 5\%$, $F2 = \cos$ like rating. Wind speed, air temperature and air humidity were measured hourly at a fixed position, 20 cm above the surface of the ground. The Testo 405-v1 hot-wire anemometer (Testo, Inc., Flanders, NJ), was used to measure the wind speed with the accuracy of $\pm 5\%$ of reading. The air temperature and air humidity were measured on an hourly basis by a DT-615 hygrothermography (CEM, Ltd., HK), which measured humidity with the accuracy of $\pm 2.5\%$ of reading and temperature with $\pm 0.5\%$. The ground surface temperature was also measured hourly by a Fluck66 handheld infrared radiometer (Fluke UK Ltd, Norwich, Norfolk), which had been calibrated for emissivity with the accuracy of $\pm 1\%$ of reading, and the emissivity of which was set as 0.95 which is suitable for sand at the spectral range from 8 to 14 μm . At 5, 10, 15, 20 and 30 cm depth, the soil temperatures were measured

hourly by bent stem mercury thermometers with the accuracy of $\pm 0.1^\circ\text{C}$.

In addition to the micro-meteorological and soil temperatures, the water content (at 10 and 30 cm depth) and the soil matric potential (at 10, 15 and 30 cm depth) were also measured hourly. The water content was measured by the Intelligent Apparatus of Measuring Soil Moisture (TSCII) with the accuracy of $\pm 2\%$ of reading, manufactured by the Institute of Sensor and Detection Technology at the University of Chinese Agriculture. The measurement of soil water content by TSCII is based on the determination of soil dielectric constant using the principle of standing-wave ratio (Zhao et al. 2002). The TSCII was installed horizontally in sand in order to minimize the disturbance of vertical coupled liquid water, water vapour and heat transport. The soil matric potential was measured by a WM-1 tensiometer with the accuracy of ± 0.13 hPa, which was manufactured by the Institute of Hydrogeology and Engineering Geology, Chinese Academy of Geological Sciences.

Field data

Figure S1 shows measured soil temperatures and water contents. The soil temperature fluctuated strongly at the soil surface, and the range of variation was 35.2°C. However, at a depth of 30 cm, there was only a small fluctuation, and the variation was only 1.8°C during the observation. Although the variation of soil temperature decreased with increasing depth, the temperature data showed a typical sinusoidal diurnal behaviour at all depths (Fig. S1).

The water content at a depth of 10 cm varied from 4.4 to 6.1% (Fig. S1). Its maximum value (5.9–6.1%) occurred at midday (0–1 p.m.), while its minimum value (4.4–4.5%) occurred before dawn (2–3 a.m.). The water content at a depth of 30 cm varied from 10.4 to 13.1% (Fig. S1). Its maximum value (11.9–13.1%) was observed in afternoon (2–3 p.m.), and its minimum value (10.4–10.8%) was observed before dawn (4–5 a.m.).

Although there are laboratory experiments (Ho and Webb 1999), which measured the water vapour diffusion in porous medium directly, it is very difficult to directly observe the water vapour transport in the field. The feasible method to measure the water vapour transport in field is the indirect method, which infers the water vapour flux from soil matric potential and soil temperature using the modified Fickian-diffusion equation (Philip 1957; Bear 1972; Miyazaki 1993; Tindall and Kunkel 1999). Figure S2 shows the diurnal variation of water vapour flux between depths of 10 and 30 cm from 4 October to 7 October 2004. The positive value indicates the upward water vapour flux. During the observation, the water

vapour transported upwards to ground level at night and in the morning (from 9–10 p.m. to 11–12 a.m.) and downwards to the deeper soil in day and early night (from 11–12 a.m. to 9–10 p.m.).

Model description

The modified HYDRUS-1D code, which refers to the coupled water, water vapour and heat transport in soil was applied in order to simulate soil water fluxes. The governing equation for one-dimensional vertical flow of liquid water and water vapour in variably saturated media is given by the following mass conservation equation (Saito et al. 2006):

$$\frac{\partial \theta}{\partial t} = -\frac{\partial q_L}{\partial z} - \frac{\partial q_v}{\partial z} \quad (1)$$

where, q_L and q_v are the flux densities of liquid water and water vapour (cm d^{-1}), respectively; t is time (days); z is the vertical axis positive upward (cm).

The flux density of liquid water, q_L , is defined as (Philip and de Vries 1957)

$$q_L = q_{Lh} + q_{LT} = -K_{Lh} \left(\frac{\partial h}{\partial z} + 1 \right) - K_{LT} \frac{\partial T}{\partial z} \quad (2)$$

where, q_{Lh} and q_{LT} are respectively the isothermal and thermal liquid water flux densities (cm d^{-1}); h is the matric potential head (cm); T is the temperature (K); and K_{Lh} (cm d^{-1}) and K_{LT} ($\text{cm}^2 \text{K}^{-1} \text{d}^{-1}$) are the isothermal and thermal hydraulic conductivities for liquid-phase fluxes due to gradients in h and T , respectively.

Using the product rule for differentiation and assuming the relative humidity in soil pores keeps constant with temperature (Philip and de Vries 1957), the flux density of water vapour, q_v , can be written as

$$q_v = q_{vh} + q_{vT} = -K_{vh} \frac{\partial h}{\partial z} - K_{vT} \frac{\partial T}{\partial z} \quad (3)$$

where, q_{vh} and q_{vT} are the isothermal and thermal water vapour flux densities (cm d^{-1}), respectively; K_{vh} (cm d^{-1}) and K_{vT} ($\text{cm}^2 \text{K}^{-1} \text{d}^{-1}$) are the isothermal and thermal water vapour hydraulic conductivities, respectively. Combining Eq. (1), (2), and (3), we obtain the governing liquid water and water vapour flow equation:

$$\begin{aligned} \frac{\partial \theta}{\partial t} &= \frac{\partial}{\partial z} \left[K_{Lh} \frac{\partial h}{\partial z} + K_{Lh} + K_{LT} \frac{\partial T}{\partial z} + K_{vh} \frac{\partial h}{\partial z} + K_{vT} \frac{\partial T}{\partial z} \right] \\ &= \frac{\partial}{\partial z} \left[K_{Th} \frac{\partial h}{\partial z} + K_{Lh} + K_{TT} \frac{\partial T}{\partial z} \right] \end{aligned} \quad (4)$$

where, K_{Th} (cm d^{-1}) and K_{TT} ($\text{cm}^2 \text{K}^{-1} \text{d}^{-1}$) are the isothermal and thermal total hydraulic conductivities, respectively, and where:

$$K_{Th} = K_{Lh} + K_{vh} \quad (5)$$

$$K_{TT} = K_{LT} + K_{vT}. \quad (6)$$

For the sake of brevity, a detailed description of the modified HYDRUS-1D code is not given here, but any interested readers are referred to Saito et al. (2006).

Soil characteristics data

The water retention curve (WRC) is one of the most fundamental hydraulic characteristics to solve the flow equation of water in soils. The soil water retention equation is given by (van Genuchten 1980)

$$\theta(h) = \begin{cases} \theta_r + \frac{\theta_s - \theta_r}{[1 + |\alpha h|]^m} & h \leq 0 \\ \theta_s & h > 0 \end{cases} \quad (7)$$

where, θ is the volumetric water content ($\text{cm}^3 \text{cm}^{-3}$) at pressure head h (cm); θ_r and θ_s are the residual and saturated water contents, respectively ($\text{cm}^3 \text{cm}^{-3}$); α (>0 , in cm^{-1}) is related to the inverse of the air-entry pressure; n (>1) is a measure of the pore-size distribution affecting the slope of the retention function ($m = 1 - 1/n$).

The characteristics of the sand used in this experiment is close to that of Wagram sand (loamy, siliceous, thermic Arenic Paleudult), which has a weak medium granular structure. The soil water retention equation (Eq. 7) was fitted to the measured water content and soil matric potential data using the inverse method, leading to $\theta_r = 0.01 \text{ cm}^3 \text{cm}^{-3}$, $\theta_s = 0.39 \text{ cm}^3 \text{cm}^{-3}$, $\alpha = 0.0316 \text{ cm}^{-1}$, and $n = 3.3$ (Fig. S3). The goodness of fit of Eq. (7) was quantified with the root mean square error (Schaap and Leij 2000):

$$\text{RMSE} = \sqrt{\frac{\sum_{i=1}^{N_w} (\theta_i - \theta'_i)^2}{N_w - n_p}} \quad (8)$$

where, N_w is the number of water retention measurements (θ - h pairs); θ and θ' are the measured and calculated water content, respectively; n_p is the number of parameters that were optimized.

Although the RMSE is 0.01 (%) for 106 in situ measured θ - h pairs, the measurements did not include the higher pressure heads ($0 \text{ cm} > h > -50 \text{ cm}$). This would cause uncertainties in representing the moist state of the experimental sand by the water retention curve. However, in this experiment, there was no precipitation and the sand bunker kept relatively dry (4.4–13.1%) during the whole observation.

Initial and boundary conditions

The soil profile was considered to be 80 cm deep. The nodes located at depths of 5, 10, 15, 20 and 30 cm were selected for comparing calculated temperatures and volumetric

water contents with measured values. The spatial discretization of 1 cm was used, leading to 81 nodes across the profile. The calculations were performed for a period of 2.5 days from 4 October to 7 October in 2004. Discretization in time is varying between a minimum and a maximum time-step, controlled by some time-step criterion (Saito et al. 2006). Except for the aforementioned geometry and time information, it is necessary to specify initial conditions for temperature and matric potential in order to solve this problem by the modified HYDRUS-1D code.

The initial matric potentials and soil temperatures were determined from measured values on 4 October by interpolating the measured values between different depths. Boundary conditions at the soil surface for liquid water, water vapour, and heat transport were determined from the meteorological data. The modified HYDRUS-1D uses the continuous meteorological data in the energy balance equation, which is calculated in order to get the surface heat flux, which is subsequently used as a known heat flux boundary condition on the soil surface. At the same time, the surface evaporation is calculated as the surface boundary condition for the soil moisture transport (Saito et al. 2006). In order to provide the values of meteorological variables at a time interval of interest for the calculation at the same or similar time intervals, relatively simple approaches were used (see Saito et al. 2006). The free drainage was considered as the bottom boundary condition and the discharge rate assigned to bottom node was determined by the program (Simunek et al. 2005). The lower boundary condition for heat transport was a Neumann type boundary condition with a zero temperature gradient.

Simulation results

In this section, the measured water contents, soil temperatures and thermal water vapour fluxes were compared with those that were calculated by the modified HYDRUS-1D code, which refers to the coupled liquid water, water vapour and heat transport in soil. The predicted and observed soil temperatures at depths of 5, 10, 15, 20 and 30 cm were shown in Fig. S4. The simulation’s goodness of fit was quantified with the following relative root mean square error measure:

$$RRMSE = \frac{\sqrt{\sum_{i=1}^{N_w} (M_i - C_i)^2 / N_w}}{\text{Max}(M_1, M_2, \dots, M_{N_w}) - \text{Min}(M_1, M_2, \dots, M_{N_w})} \quad (9)$$

where, N_w is the number of the measurements; M_i and C_i are measurements and calculations, respectively; $\text{Max}(M_1,$

$M_2, \dots, M_{N_w})$ and $\text{Min}(M_1, M_2, \dots, M_{N_w})$ are the maximum and minimum value of the measurements. The RRMSE is dimensionless and $RRMSE = 0$ indicates the best fit. The smaller is the RRMSE, the better the fit of simulation.

The RRMSEs of the temperature at depths of 5, 10, 15, 20 and 30 cm were respectively 0.094, 0.108, 0.152, 0.184 and 0.199. Although there were spiky points at depths of 15 and 20 cm, simulated and measured temperatures generally agreed at all five depths and both showed typical sinusoidal diurnal variation, with the maximum absolute deviation of 5.794°C at 20 cm depth.

Figure S5 depicts simulated and measured soil water content at two depths. As seen, there is a discrepancy between the observed and simulated water contents. The RRMSEs of the water content at depths of 10 and 30 cm are 0.289 and 0.211, respectively. At 10 cm depth, the simulated water content can follow the general trend of observation merely; while at 30 cm depth, the simulation shows a decreasing trend instead of a variation like the measurement has. However, apart from the poor fit of the simulation to the trend of water content variation at 30 cm depth, the mean of the simulated water contents is close to that of the measurements. The means of simulated and observed water contents are 5.002 and 5.076% at 10 cm depth, and 11.222 and 11.236% at 30 cm depth, respectively. Furthermore, the average relative errors at depths of 10 and 30 cm are 1.022 and 1.001; both are close to 1. It indicated that the simulated water contents could fit the most of measured values fairly well. The average relative error is defined as (Kleijnen et al. 2001)

$$AVRE = \sum (C_i/M_i)/N_w \quad (10)$$

where, the symbols were the same as in Eq. (9).

Calculated thermal water vapour fluxes were compared with the measurements shown in Fig. S6. The predicted thermal water vapour fluxes followed fairly well the measured values and the RRMSE is 0.111. To summarize, the modified HYDRUS-1D code could be applied in the analysis of coupled liquid water, water vapour and heat transport in this experiment.

Discussion

Numerical modelling of isothermal and non-isothermal liquid and water vapour flow plays a critical role in evaluating the physical processes, that governing soil heating, spatial distribution of water, and gaseous exchange between the soil and the atmosphere. In this section, the modified HYDRUS-1D code was used to produce the hourly profiles of isothermal and non-isothermal water vapour fluxes, liquid water fluxes and soil temperatures from 4 October to

7 October 2004. Then, an interpolation and smoothing program (SURFER) was used to create continuous three-dimensional fields for the diurnal pattern interpretation of soil water dynamics. The three dimensional fields consisted of a space–time field (two-dimensional field) and a dependent specific flux or temperature (third dimension). Finally, the basic soil water dynamics were conceptualized with a schematic figure.

Temperature and temperature gradients fields

In order to understand the diurnal variation and the mechanism of heating of the soil, there is a need to look at the temperature variation in the soil profile. The contour chart of temperature, in Fig. 1, shows the hourly variation of soil temperature profiles. Where, the interval of contours was 2°C.

Before 7 a.m. 5 October, the contours at the surface were sparse and the surface temperature varied slowly with the rate of 0.53°C per hour. From 7 a.m. to 7 p.m. 5 October, the contours became dense and the surface temperature fluctuated strongly with the rate of 5.2°C per hour. During this period, the surface temperature increased from

7.4°C at 7 a.m. to the highest value of 42°C at 1 p.m., and dropped to 14°C at 7 p.m., which was the changing point for the contours that varied from denseness to sparseness.

From 7 p.m. 5 October to 6 a.m. 6 October, the contours were sparse again and the variations of the surface temperature were reduced. In this period, the surface temperature changed from 14°C (at 7 p.m. 5 October) to 8.2°C (at 6 a.m. 6 October) with the rate of 0.52°C per hour. After 6 a.m., the contours would experience the period of denseness again, in which the surface temperature varied strongly. It was important to note that the denseness and sparseness indicated the rapid variation and slow variation of soil temperature, respectively.

As shown in Fig. 1a, the density of contours decreased with depth. It indicated that the variation of soil temperature was reduced with depth. During the observation period, the surface temperature varied from 6.8 to 42°C, while from 17 to 18.8°C at depth of 30 cm. At a depth of 40 cm, the variation of temperature was less than 0.3°C. Note that, since the variation of temperature was close to zero below a depth of 40 cm, the soil temperature profile information below a depth of 40 cm depth is not shown herein.

Figure 1b shows the space–time temperature gradient field, which clearly shows how heat transport in soil controls the dependence of the temperature gradient profiles in time and space. The temperature gradients were derived from $\Delta T = (T_{i+1} - T_i)$ (°C cm⁻¹), where T_i represented the soil temperature at a depth of i cm. The variation of contours in Fig. 1b was accordant with that in Fig. 1a. The contours experienced alternatively the sparseness and denseness with time released, and developed downwards from denseness to sparseness with depth.

From temperature gradient profiles, it was seen that there was an active layer for heat exchange, which was about 10 cm thick right below the ground surface. Between depths of 0 and 1 cm, the temperature gradient could reach 6.9°C cm⁻¹. At a depth of 10 cm, the gradients were between 0 and 0.6°C cm⁻¹, and there was very small temperature gradient below depths greater than 10 cm. In addition, there were five contours for the temperature gradient of 0°C cm⁻¹, which indicated no heat conduction in the space–time field. Accordingly, these five contours were defined as zero heat flux planes.

There were two types of zero heat flux planes: one was the divergent plane, where the temperature gradient, above and below this plane, respectively was positive and negative (upwards and downwards); the other was the convergent plane, where the directions of the temperature gradient were completely reversed (i.e. downwards and upwards) compared with those to the divergent plane. During the whole observation, there were three divergent zero heat flux planes and two convergent zero heat flux

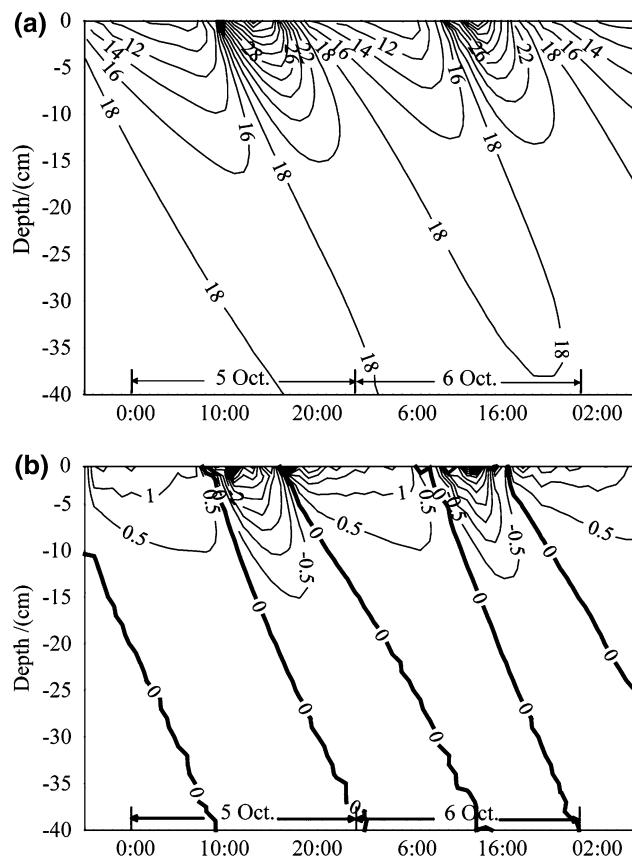


Fig. 1 Distributions of soil temperatures (a) and temperature gradients (b) in space and time

planes. The zero heat flux plane could be regarded as the ‘changing point’, i.e. the point at which the direction of the temperature gradient reversed. The divergent planes started in afternoon (4–5 p.m.), while the convergent planes happened in morning (6–8 a.m.).

Non-isothermal flux fields

The non-isothermal liquid water (q_{LT}) and water vapour (q_{vT}) fluxes are controlled not only by the temperature gradient, but also by the thermal liquid (K_{LT}) and water vapour (K_{vT}) hydraulic conductivities. The functions for the thermal hydraulic conductivities are defined as (Noborio et al. 1996; Fayer 2000):

$$K_{LT} = K_{Lh} \left(hG_{wT} \frac{1}{\gamma_0} \frac{d\gamma}{dT} \right) \tag{11}$$

$$K_{vT} = \frac{D}{\rho_w} \eta H_r \frac{d\rho_{sv}}{dT} \tag{12}$$

where, K_{Lh} is the isothermal unsaturated hydraulic conductivity (cm d^{-1}), which is decided by the van Genuchten’s (1980) model; G_{wT} is the gain factor (dimensionless), which assesses the temperature dependence of the soil water retention curve and is set as 7 for sand (Noborio et al. 1996); γ is the surface tension of soil water (J cm^{-2}), and γ_0 is the surface tension at 25°C (J cm^{-2}); D is the water vapour diffusivity in soil ($\text{cm}^2 \text{d}^{-1}$); η is the enhancement factor (dimensionless); ρ_w is the density of liquid water (g cm^{-3}); ρ_{sv} is the saturated water vapour density (g cm^{-3}); H_r is the relative humidity (dimensionless) and is expressed as $\text{EXP}(hMg/RT)$; M is the molecular weight of water (g mol^{-1}); g is the gravitational acceleration (m s^{-2}); R is the universal gas constant ($\text{mol}^{-1} \text{K}^{-1}$).

Figure S7a shows the variations of the thermal liquid hydraulic conductivity profiles in the space–time field. The K_{LT} increased with depth and kept this trend during the whole observation period. However, the temporal variation of K_{LT} was not uniform throughout the profile. Above a depth of 13 cm, K_{LT} only varied slightly with time: the extent of variation was from 0.009 to 0.024 ($\text{cm}^2 \text{K}^{-1} \text{d}^{-1}$) and the maximum changing rate was 0.0007 ($\text{cm}^2 \text{K}^{-1} \text{d}^{-1}$) per hour. However, below a depth of 13 cm it started to drop rapidly with time. Where, the maximum rate of decrease was 0.005 ($\text{cm}^2 \text{K}^{-1} \text{d}^{-1}$) per hour, and the extent of variation was from 0.041 to 0.296 ($\text{cm}^2 \text{K}^{-1} \text{d}^{-1}$).

The thermal water vapour hydraulic conductivities (Fig. S7b) experienced a different trend throughout the profile. Below a depth of 15 cm, the K_{vT} decreased with depth, compared to the increase of K_{LT} with depth. Although the temporal variation of the K_{vT} profile was also inconsistent, the character of it was completely different

from the K_{LT} profile. The K_{vT} fluctuated strongly from 0.005 to 0.661 ($\text{cm}^2 \text{K}^{-1} \text{d}^{-1}$) with time, between depths of 0 and 15 cm, compared to the small variation of K_{LT} at the same soil layer; besides, below a depth of 15 cm, the K_{vT} went through a slow variation, compared to the rapid variation of K_{LT} .

From the comparison, although the variation of the K_{vT} and K_{LT} in space–time field was almost opposite, they were of about the same order of magnitude. However, K_{vT} varied stronger than K_{LT} , especially, in the shallow layer right below the ground surface (between the depths of 0 and 15 cm). It indicated that the non-isothermal water vapour flow was more important in the upper soil layer. In addition, the variation of K_{vT} also denoted its higher sensitivity to the temperature variation than that of K_{LT} .

The space–time fields of non-isothermal liquid and water vapour fluxes were shown in Fig. 2. Corresponding to the zero heat flux planes in Fig. 1b, the q_{LT} and q_{vT} field had the zero thermal liquid flux planes (Fig. 2a) and the zero thermal water vapour flux planes (Fig. 2b), both of which were sub-classified into divergent and convergent planes according to the definitions of zero heat flux planes. The downward propagation of the zero thermal

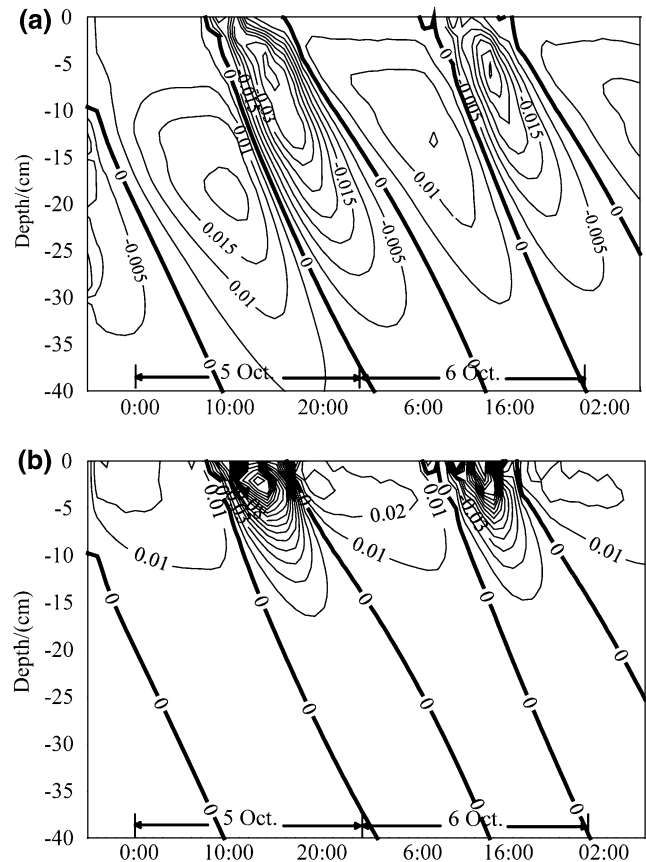


Fig. 2 Distributions of the thermal liquid fluxes (a) and the thermal water vapour fluxes (b) in space and time

liquid and the water vapour flux planes were accordant with that of the zero heat flux planes over the simulation period.

There were ellipses between the planes of divergence and convergence in both q_{LT} and q_{vT} fields. The ellipses in q_{LT} field were much more obvious than those in q_{vT} field. The occurrence of ellipses was dependent on the thermal liquid and water vapour fluxes profiles. According to the q_{LT} field (Fig. 2a), there were three types of liquid flux profiles:

1. The first type occurred before dawn (1–7 a.m.). During this period, there were only the divergent planes existed in the profile. After 7 a.m., the plane of divergence had almost reached a depth of 40 cm, and liquid flux was upward almost throughout the entire profile above 40 cm. In addition, the bulge of thermal liquid flux moved deeper and deeper with time and the peak flux increased with time, which varied from 0.012 cm d^{-1} at 1 a.m. to 0.02 cm d^{-1} at 7 a.m. (Fig. 3a). The increasing upward flux showed that liquid water in deeper soil was drawn to the surface layer at night by a temperature gradient. The propagation of the bulge of fluxes indicated the formation of the ellipses in Fig. 2a;
2. There were only the convergent planes of zero thermal liquid flux that existed in the second type profile. The directions of the thermal liquid fluxes were opposite to those in the first type. The propagation of the bulge of fluxes was accordant with that in type one, but the direction was reversed; the peak flux varied from -0.036 cm d^{-1} at 8 a.m. to -0.04 cm d^{-1} at 5 p.m. (Fig. 3b). The second type profiles happened during the day (8 a.m.–5 p.m.), where the convergent plane reached the depth of 24 cm. This indicated that the downward flow of the thermal liquid water occurred during day and in the top $\sim 24 \text{ cm}$; below a depth of 24 cm, the liquid water was upward and the peak flux decreased from 0.022 to 0.009 cm d^{-1} ;
3. The third type profile was the transition between the first type and the second type. Both the divergent planes and convergent planes were seen in this profile. The divergent plane was above the convergent plane, which indicated that the profile was changing from the second type to the first type. The third type profile occurred before midnight (6–12 p.m.). During this period, the divergent plane moved from the surface to -15 cm , and the convergent plane moved from -25 to -38 cm . This indicated that the liquid water flux in the top layer (above -25 cm) started to be upward and

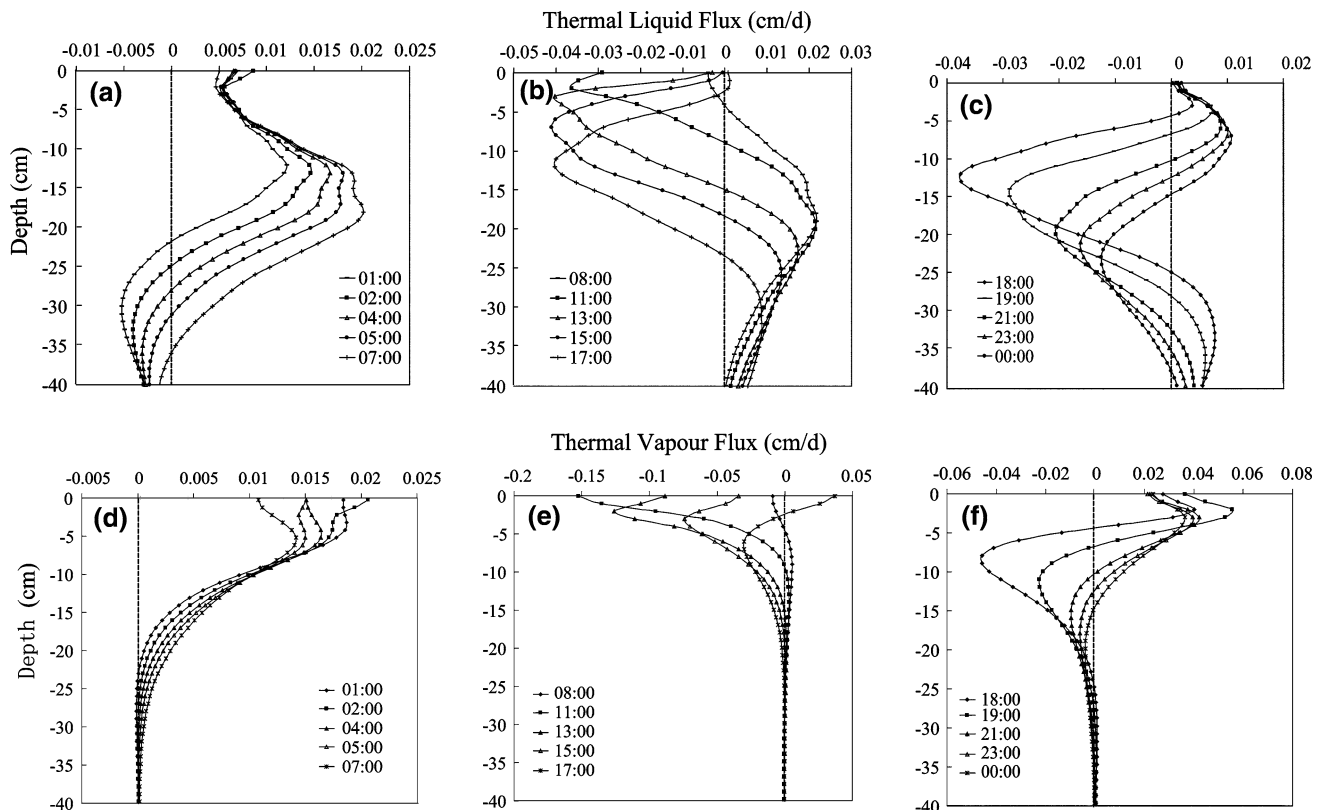


Fig. 3 Different types of thermal liquid flux profiles (a, b, c) and thermal water vapour flux profiles (d, e, f)

increased after 6 p.m., from 0.004 to 0.01 cm d⁻¹; below -25 cm, the liquid water flux started to decrease from 0.008 to 0.001 cm d⁻¹ (Fig. 3c). After the upward peak flux at greater depth reached zero, the flux profile became the first type again.

As for the space–time field of the thermal water vapour flux (Fig. 2b), there were three corresponding types of water vapour flux profiles, compared with those in *qLT* field. From the thermal water vapour flux profiles, it was seen that the bulges of water vapour fluxes, above -20 cm, fluctuated from 0.061 to -0.177 cm d⁻¹ throughout all profiles (from Fig. 3d–f); below -20 cm, the fluctuation of the bulge of flux was small and varied from 0.003 to -0.004 cm d⁻¹.

The range of variation for the thermal water vapour flux was 0.238 cm d⁻¹ above -20 cm and 0.009 cm d⁻¹ at greater depth, and the corresponding variation range of the thermal liquid flux was 0.063 and 0.042 cm d⁻¹. The variation of thermal water vapour flux was one order of magnitude more than that of the thermal liquid flux in the subsurface layer, while one order of magnitude less than that in deeper layer. It indicated that the thermal water vapour flux dominated in the top ~20 cm, while the thermal liquid flux dominated at greater depth.

As shown in Fig. 3d, the flow of thermal water vapour was upward throughout the entire profile after 5 a.m., which indicated that the evaporation in soil occurred before dawn (1–7 a.m.). The second type of thermal water vapour flux profile was showed in Fig. 3e, and the thermal water vapour flux was moving downward in day (from 8 a.m. to 5 p.m.). The transition type profile of the thermal water vapour flux was not obvious due to the small variation of the water vapour flux at greater depth (Fig. 3f). Thus, the maximum thermal water vapour flux was only 0.003 cm d⁻¹ below the plane of convergence. However, it was still seen that the evaporation started to develop from the uppermost soil to the deeper soil, and that the thermal water vapour flux was changing from the second type to the first type.

Matric potential and its gradient field

The total soil water potential reflects the energy state of water in porous media and subsequently influences the flow of liquid water and water vapour in the vadose zone. Direction of water movement can be determined using potential gradients in soil, because water moves from regions of high kinetic energy to regions of low kinetic energy (Jury et al. 1991). Gravitational potential is equal to the elevation above (positive) or below (negative) a datum. In this case, the ground surface is regarded as the datum and the gravitational potential is negative; for example, the

gravitational potential at the depth of 5 cm is -5 cm. Matric potential represents the driving force related to the matrix. Osmotic potential results from the difference in the concentration of the pore water. However, there is no solute considered. Then, the total water potential includes only matric and gravitational potential in this case. It is necessary to understand how the soil matric potential varies in space and time field.

The hourly variation of matric potential profile was shown in Fig. 4a. The interval of the contours was -10 cm (water column). From Fig. 4a, the matric potential was lowest near the surface and increased with depth, which indicated that there was an upward driving force for liquid water and water vapour during the whole simulation period. The matric potential fluctuated from -3084 to -94.109 cm at surface, while varied from -54.582 to -49.26 cm at -40 cm. The rapid variation of the matric potential happened from 10 a.m. to 11 p.m., and was restricted to the uppermost soil layer.

Figure 4b shows the distribution of the matric potential gradient in space and time. The interval of the contours was 0.2 cm per cm. The potential gradients were decided by $\Delta h = (h_{i+1} - h_i)$ (cm cm⁻¹), where h_i represented the soil

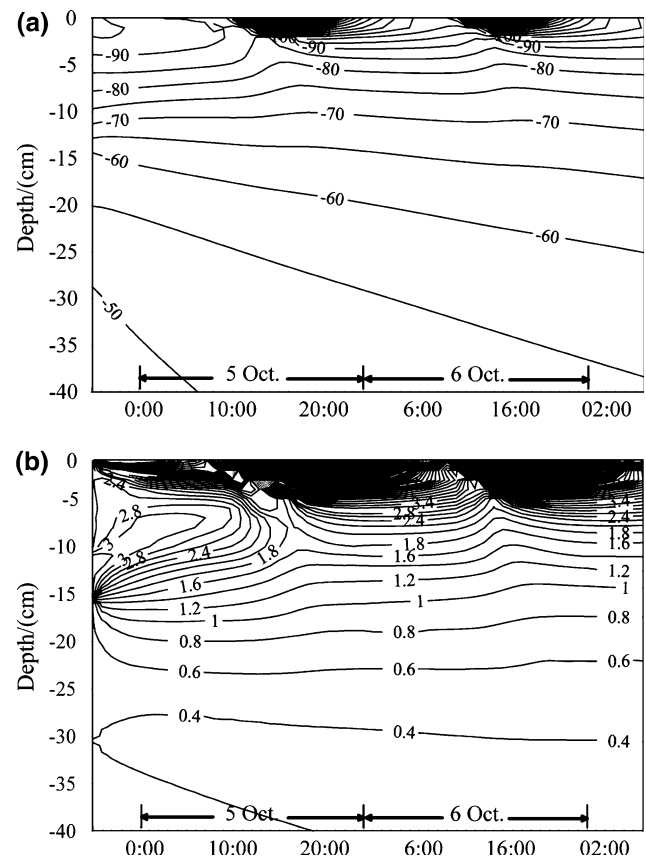


Fig. 4 Distributions of the matric potentials (a) and the matric potential gradients (b) in space and time

matric potential at a depth of i cm. From Fig. 4b, it was seen that the contours in the soil layer, between 0 and -5 cm, was most intensive, which indicated the fluctuation of the matric potential gradient was strongest near the surface. The gradient varied from 2923.627 to 1.027 cm cm^{-1} at surface, and varied from 4.229 to 1.281 cm cm^{-1} at -5 cm. The top 5-cm layer could be regarded as the active layer for the isothermal flux driven by the matric potential. Below -5 cm, the variation of the gradient tended to be steady, except for the occurrence of the bulge of gradient in the initial period. The matric potential gradient was positive throughout the entire profile.

Isothermal flux fields

The variation of the isothermal water vapour flux was shown in Fig. 5a. From the flux profiles, it was seen clearly how the matric potential determines the dependence of isothermal water vapour on space and time. In the top ~ 5 cm layer, the fluctuation was strong. The isothermal water vapour flux varied from 4.018×10^{-4} to

6.749×10^{-9} cm d^{-1} at surface, and from 2.365×10^{-7} to 5.132×10^{-8} cm d^{-1} at -5 cm. At deeper soil layers, there was almost no fluctuation. For example, at -40 cm, the maximum flux was 5.309×10^{-9} cm d^{-1} and the minimum flux was 1.743×10^{-11} cm d^{-1} . During the whole simulation period, the direction of the isothermal water vapour flux was upwards throughout the entire profile (Fig. 5c).

Although the matric potential gradient was upwards throughout the entire profile during the simulation period, the isothermal liquid water flux was not only upward, but also downward in the space–time filed (Fig. 5b). There was a reversal in the direction from upward to downward. From the isothermal liquid flux profiles, there was a plane of divergence developed from -16 cm that fluctuated between -13 and -17 cm. The reason for this was the isothermal liquid water was driven not only by the matric potential gradient, but also the gravitational gradient. The gravitational gradient was -1 cm cm^{-1} between two nodes. When the matric potential gradient was larger than 1 cm cm^{-1} , the flux of the isothermal liquid water would be upward. Otherwise, the matric potential would be

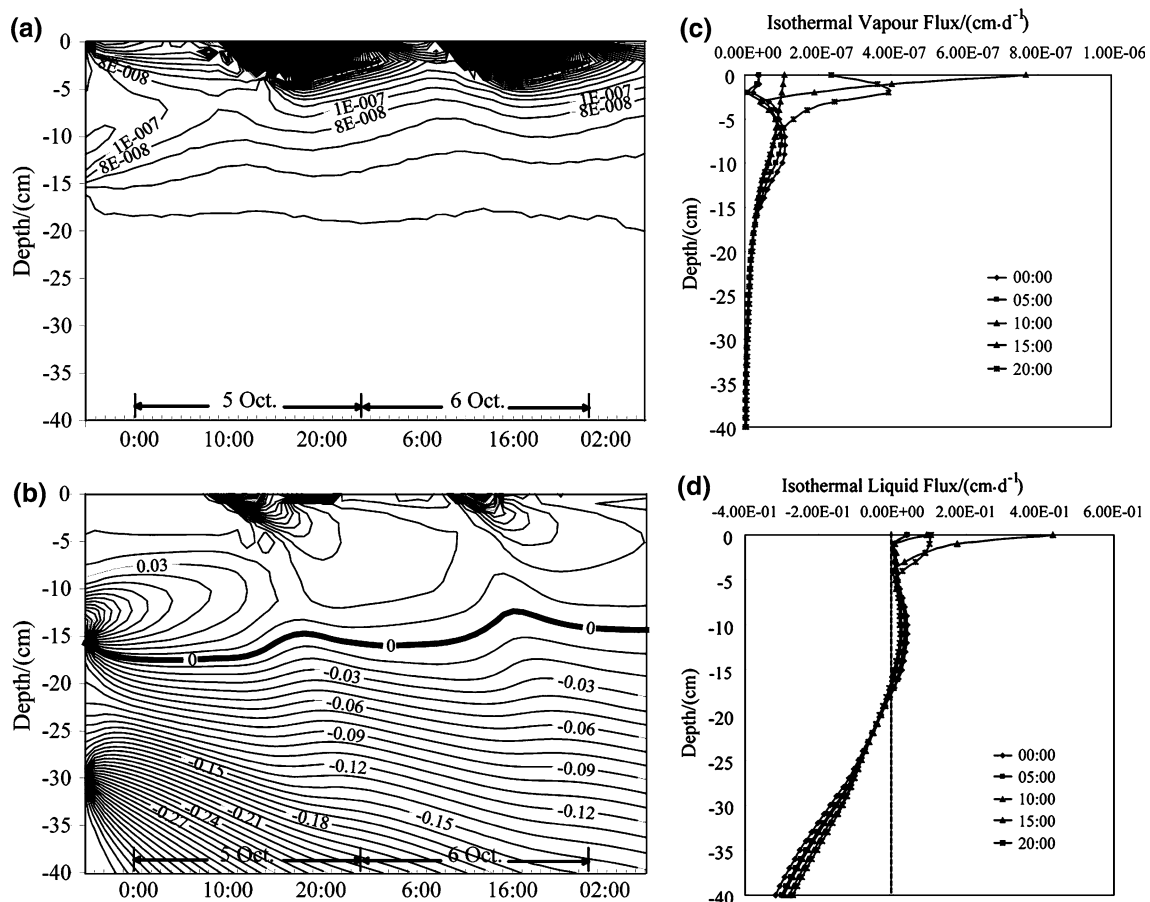


Fig. 5 Distribution of the isothermal water vapour fluxes (a) and the isothermal liquid fluxes (b) in space and time; Isothermal water vapour flux profiles (c) and isothermal liquid flux profiles (d)

smaller than the gravitational potential and the flux of the isothermal liquid water would be downward. In the matric potential gradient field, there was a plane with the gradient of 1 cm cm^{-1} , which fluctuated between -13 and -17 cm . It was accordant to the fluctuation of the plane of divergence in Fig. 5b. The isothermal liquid water flux was upward above the plane of divergence, while downward below the plane, during the whole simulation period (Fig. 5d).

Soil water dynamics

Generally, three stages could be recognized from the spatial–temporal distributions of liquid water flux and water vapour flux (Fig. 6). Due to the isothermal flux profiles kept fixed during the whole simulation period, the determination of the stages was corresponding to the occurrences of the three types of thermal flux profiles. The isothermal water vapour flux was upward through all three stages, and it was at least two orders of magnitude less than other fluxes. Considering its stability and small magnitude, the isothermal water vapour flux would not be discussed in these specific stages.

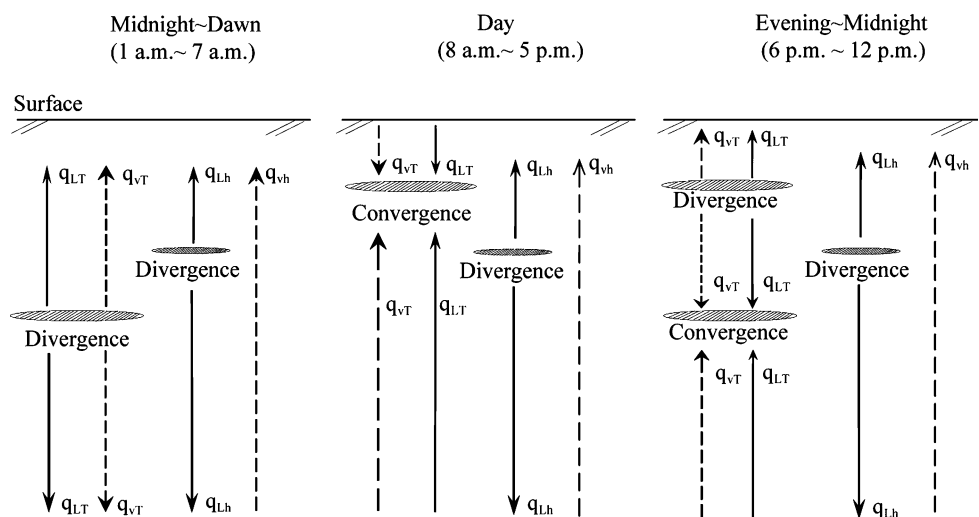
The first stage started from midnight and ended before dawn (1–7 a.m.) (Fig. 6). During this stage, the isothermal liquid flux, the thermal liquid and water vapour flux were upward above the plane of divergence, and downward below this plane. The magnitude of the upward value of thermal water vapour flux ($0.238\text{--}0.0007 \text{ cm d}^{-1}$) was similar with that of thermal liquid flux ($0.202\text{--}0.0002 \text{ cm d}^{-1}$). Compared to the thermal liquid and water vapour flux, the isothermal liquid flux ($0.064\text{--}0.0001 \text{ cm d}^{-1}$) was less significant in this stage. However, below the divergent plane, the downward isothermal liquid flux (-0.329 to -0.378 cm d^{-1}) dominated, while the thermal water vapour

flux ($-2.146 \times 10^{-6}\text{--}3.833 \times 10^{-4} \text{ cm d}^{-1}$) was most insignificant. The plane of divergence developed from -23 cm at the beginning of this stage and propagated downward to -36 cm at the end. This stage indicated that the upward thermal flux dominated in the upper soil layer, while the downward isothermal flux dominated in the deeper soil layer.

The second stage was in day between 8 a.m. and 5 p.m. In this stage, the plane of convergence occurred at -3 cm and moved downward to the depth of 24 cm . Above the convergent plane, the magnitude of the downward thermal water vapour flux (-0.244 to $-2.409 \times 10^{-3} \text{ cm d}^{-1}$) was larger than the thermal liquid flux (-0.04 to $-5.509 \times 10^{-5} \text{ cm d}^{-1}$). However, the thermal water vapour flux was not the dominant flux. The magnitude of upward isothermal liquid flux ($0.423\text{--}0.029 \text{ cm d}^{-1}$) exceeded the thermal flux above the convergent plane. In addition, the downward isothermal liquid flux was over the upward thermal flux below the convergent plane. It indicated that the isothermal liquid flux dominated during day throughout the entire profile.

The third stage was from evening to midnight (6–12 p.m.). It was the transition stage between the second stage and the first stage. The plane of divergence started from -5 cm and ended at -15 cm . In the initial period of this stage (6–7 p.m.), the upward isothermal liquid flux was over the thermal flux above the divergent plane. In the top $\sim 5 \text{ cm}$ soil layer, the average of the isothermal liquid flux was 0.033 cm d^{-1} , compared with 0.031 cm d^{-1} of thermal water vapour flux and 0.004 cm d^{-1} of thermal liquid flux. During the rest of this stage, the average of the thermal water vapour flux (0.022 cm d^{-1}) was close to the average isothermal liquid flux (0.021 cm d^{-1}) and over the average thermal liquid flux (0.005 cm d^{-1}). The plane of convergence occurred at -24 cm and developed downward to

Fig. 6 Schematic illustration of the diurnal soil water dynamics



–38 cm. The direction of the thermal liquid flux, thermal water vapour flux and isothermal liquid flux were the same between –15 and –24 cm; however, the isothermal liquid flux was dominant in this soil layer. Below –24 cm, the downward isothermal liquid flux was still the most dominant type of flux. During this transition stage, the dominant flux in the top ~5 cm soil layer changes from the isothermal liquid flux to the thermal water vapour flux; at the mean time, the isothermal kept the dominance at greater depth. It indicated that the third stage was changing toward the situation in the first stage.

Conclusion

The modified HYDRUS-1D code, which refers to the coupled transport of liquid water, water vapour and heat, could be applied to further evaluate the mechanisms affecting unsaturated flow at the site. It was convenient to use the space–time fields to investigate the propagation of the heat and water flow in soil. According to the space–time fields of the non-isothermal and isothermal flux, three stages of the soil water dynamics were determined. Generally, the thermal water vapour and liquid flux was dominant in uppermost soil layer at night, while the isothermal liquid water dominated during the day and in the deeper soil layer. The numerical simulations suggested that the isothermal liquid flux, the non-isothermal liquid flux and the non-isothermal water vapour flux should be considered in the conceptualization of the unsaturated flow in soil. Although this study was for the relative coarse sand in the sand bunker, further studies for sand in natural conditions (particularly in desert) are necessary.

References

- Agam N, Berliner PR (2006) Dew formation and water vapor adsorption in semi-arid environments—a review. *J Arid Environ* 65(4):572–590
- Agam N, Berliner PR, Zangvil A, Ben-Dor E (2004) Soil water evaporation during the dry season in an arid zone. *J Geophys Res* 109:161–173
- Asghar MN (1996) Computer simulation of salinity control by means of an evaporative sink. Ph. D Thesis, University of Newcastle upon Tyne
- Athavale RN, Rangarajan R, Muralidharan D (1998) Influx and efflux of moisture in a desert soil during a 1 year period. *Water Resour Res* 34(11):2871–2877
- Bear J (1972) Dynamics of fluid in porous media. Dover, New York
- Braud I, Dantasantonino AC, Vauclin M, Thony JL, Ruelle P (1995) A simple soil–plant–atmosphere transfer model (Sispat) development and field verification. *J Hydrol* 166(3–4):213–250
- Cary JW (1963) Onsager's relation and the non-isothermal diffusion of water vapor. *J Phys Chem* 67(1):126–129
- Cary JW (1964) An evaporation experiment and its irreversible thermodynamics. *Int J Heat Mass Transf* 7:531–538
- Cary JW (1965) Water flux in moist soil: thermal versus suction gradients. *Soil Sci* 100(3):168–175
- Cary JW (1966) Soil moisture transport due to thermal gradients: practical aspects. *Soil Sci Soc Am Proc* 30:428–433
- Cary JW (1979) Soil heat transducers and water vapor flow. *Soil Sci Soc Am J* 43(5):835–839
- Cary JW, Taylor SA (1962a) Thermally driven liquid and vapor phase transfer of water and energy in soil. *Soil Sci Soc Am Proc* 26:417–420
- Cary JW, Taylor SA (1962b) The interaction of the simultaneous diffusions of heat and water vapor. *Soil Sci Soc Am Proc* 26:413–416
- Vries De (1958) Simultaneous transfer of heat and moisture in porous media. *Trans Am Geophys Union* 39(5):909–916
- Dickinson RE, Oleson KW, Bonan G, Hoffman F, Thornton P, Vertenstein M, Yang Z, Zeng X (2006) The community land model and its climate statistics as a component of the community climate system model. *J Clim* 19(11):2302–2324
- Entekhabi D, Njoku E, Houser P, Spencer M, Doiron T, Smith J, Girard R, Belair S, Crow W, Jackson T (2004) The Hydrosphere State (HYDROS) mission concept: an earth system pathfinder for global mapping of soil moisture and land freeze/thaw. *IEEE Trans Geosci Remote Sens* 42(10):2184–2195
- Fayer MJ (2000) UNSAT-H Version 3.0: unsaturated soil water and heat flow model—theory, user manual and examples. Pacific Northwest National Laboratory, Washington, p 331
- Gowing JW, Konukcu F, Rose DA (2006) Evaporative flux from a shallow watertable: the influence of a vapour–liquid phase transition. *J Hydrol (Amsterdam)* 321:77–89
- Grifoll J, Cohen Y (1999) A front-tracking numerical algorithm for liquid infiltration into nearly dry soils. *Water Resour Res* 35(8):2579–2585
- Grifoll J, Gast JM, Cohen Y (2005) Non-isothermal soil water transport and evaporation. *Adv Water Resour* 28:1254–1266
- Groenevelt PH, Kay BD (1974) On the interaction of water and heat transport in frozen and unfrozen soils: II. The liquid phase. *Soil Sci Soc Am Proc* 38:400–404
- Gustafsson AM, Lindblom J (2001) Underground condensation of humid air—a solar driven system for irrigation and drinking-water production. Master Thesis 2001:140 CIV, Luleå University of Technology, Sweden
- Hauserr B, Ruess K (1993) Seawater desalination and irrigation with moist air. Ingenieurbüro Ruessund Hauserr, Switzerland
- Ho CK, Webb SW (1999) Enhanced vapor-phase diffusion in porous media—LDRD final report. USDOE. Sandia National Laboratories, Albuquerque
- Jackson RD (1973) Diurnal changes in soil water content during drying. Field soil water regime, Madison
- Jacobs AFG, Heusinkveld BG (2000) Force-restore technique for ground surface temperature and moisture content in a dry desert system. *Water Resour Res* 36(5):1261–1268
- Jacobs AFG, Heusinkveld BG, Berkowicz SM (1999) Dew deposition and drying in a desert system: a simple simulation model. *J Arid Environ* 42:211–222
- Jury WA, Gardner WR, Gardner WH (1991) Soil physics. Wiley, New York, p 328
- Kay BD, Groenevelt PH (1974) On the interaction of water and heat transport in frozen and unfrozen soils: I. Basic theory: the vapor phase. *Soil Sci Soc Am Proc* 38:395–400
- Kemp PR, Reynolds JF, Pachepsky Y, Chen JL (1997) A comparative modeling study of soil water dynamics in a desert ecosystem. *Water Resour Res* 33(1):73–90
- Kerr YH, Waldteufel P, Wigneron JP, Martinuzzi J, Font J, Berger M (2001) Soil moisture retrieval from space: the Soil Moisture and Ocean Salinity (SMOS) mission. *Geoscience and remote sensing. IEEE Trans Geosci Remote Sens* 39(8):1729–1735

- Kleijnen JPC, Cheng RCH, Bettonvil B (2001) Validation of trace-driven simulation models: bootstrap tests. *Manage Sci* 47(11):1533–1538
- Kondo J, Okusa N (1990) A simple numerical prediction model of nocturnal cooling in a basin with various topographic parameters. *J Appl Meteorol* 29(7):604–619
- Kondo J, Saigusa N, Sato T (1992) A model and experimental-study of evaporation from bare-soil surfaces. *J Appl Meteorol* 31(3):304–312
- Konukcu F, Istanbuluoglu A, Kocaman I (2004) Determination of water content in drying soils: incorporating transition from liquid phase to vapour phase. *Aust J Soil Res* 42(1):1–8
- Lindblom J, Nordell B (2006) Water production by underground condensation of humid air. *Desalination* 189:248–260
- Milly PC (1982) Moisture and heat transport in hysteretic, inhomogeneous porous media: a matrix head-based formulation and a numerical model. *Water Resour Res* 18(3):489–498
- Milly PC (1984a) Linear analysis of thermal effects on evaporation from soil. *Water Resour Res* 20(8):1075–1085
- Milly PC (1984b) Simulation analysis of thermal effects on evaporation from soil. *Water Resour Res* 20(8):1087–1098
- Milly PC (1996) Effects of thermal vapor diffusion on seasonal dynamics of water in the unsaturated zone. *Water Resour Res* 32(3):509–518
- Milly PCD, Eagleson PS (1980) The coupled transport of water and heat in a vertical soil column under atmospheric excitation, Massachusetts Institute of Technology, Department of Civil Engineering, Ralph M. Parsons Laboratory for Water Resources and Hydrodynamics
- Miyazaki T (1993) Water flow under the effects of temperature gradients. *Water Flow Soils* 169–196
- Mmolawa K, Or D (2003) Experimental and numerical evaluation of analytical volume balance model for soil water dynamics under drip irrigation. *Soil Sci Soc Am J* 67(6):1657–1671
- Nassar IN, Horton R (1997) Heat, Water, and solution transfer in unsaturated porous media: I—Theory development and transport coefficient evaluation. *Transport in Porous Media* 27(1):17–38
- Noborio K, McInnes KJ, Heilman JL (1996) Two-dimensional model for water, heat, and solute transport in furrow-irrigated soil: II. Field evaluation. *Soil Sci Soc Am J* 60(4):1010–1021
- Philip JR (1957) Evaporation, and moisture and heat fields in the soil. *J Atmos Sci* 14(4):354–366
- Philip JR, De Vries VD (1957) Moisture movement in porous materials under temperature gradient. *Trans Am Geophys Union* 38(2):222–232
- Rose DA (1963a) Water movement in porous materials: Part 1—Isothermal vapour transfer. *Br J Appl Phys* 14(5):256–262
- Rose DA (1963b) Water movement in porous materials: Part 2—The separation of the components of water movement. *Br J Appl Phys* 14(8):491–496
- Rose DA (1968a) Water movement in dry soils: 1. Physical factors affecting sorption of water by dry soil. *J Soil Sci* 19(1):81–93
- Rose DA (1968b) Water movement in porous materials. 111. Evaporation of water from soil. *Br J Appl Phys* 2(1):1779–1791
- Rose DA (1971) Water movement in dry soils. II. An analysis of hysteresis. *J Soil Sci* 22(4):490–507
- Rose DA, Konukcu F, Gowing JW (2005) Effect of watertable depth on evaporation and salt accumulation from saline groundwater. *Aust J Soil Res* 43(5):565–573
- Saito H, Simunek J, Mohanty BP (2006) Numerical analysis of coupled water, vapor, and heat transport in the vadose zone. *Vadose Zone J* 5(2):784–800
- Salzmann W, Bohne K, Schmidt M (2000) Numerical experiments to simulate vertical vapor and liquid water transport in unsaturated non-rigid porous media. *Geoderma* 98(3):127–155
- Scanlon BR (1992) Evaluation of liquid and vapor water flow in desert soils based on chlorine 36 and tritium tracers and nonisothermal flow simulations. *Water Res Res* 28(1):285–297
- Scanlon BR, Milly PCD (1994) Water and heat fluxes in desert soils 1. Field studies. *Water Resour Res* 30(3):709–720
- Schaap MG, Leij FJ (2000) Improved prediction of unsaturated hydraulic conductivity with the Mualem-van Genuchten model. *Soil Sci Soc Am J* 64(3):843–851
- Schelde K, Thomsen A, Heidmann T, Schjoenning P, Jansson PE (1998) Diurnal fluctuations of water and heat flows in a bare soil. *Water Resour Res* 34(11):2919–2929
- Shiklomanov IA, Gu W, Lu J (2004) Experimental research on the role of dew in arid ecosystem of Gobi desert, Inner Mongolia [A]. A A Balkema Publishers, Amsterdam
- Shurbaji ARM, Phillips FM (1995) A numerical-model for the movement of H₂O, H-2 O-18, and (Hho)-H-2 in the unsaturated zone. *J Hydrol* 171(1–2):125–142
- Simunek J, Sejna M, van Genuchten MT (2005) The HYDRUS-1D Software package for simulating the one-dimensional movement of water, heat, and multiple solutes in variably-saturated media. University of California, Riverside, Research reports, pp 240
- Starr JL, Paltineanu IC (1998) Soil water dynamics using multisensor capacitance probes in nontraffic interrows of corn. *Soil Sci Soc Am J* 62(1):114–122
- Starr JL, Timlin DJ (2004) Using high-resolution soil moisture data to assess soil water dynamics in the vadose zone. *Vadose Zone J* 3(3):926–935
- Taylor SA, Cary JW (1964) Linear equations for the simultaneous flux of matter and energy in a continuous soil system. *Soil Sci Soc Am J* 28:167–172
- Taylor SA, Stewart GL (1960) Some thermodynamic properties of soil water. *Soil Sci Soc Am Proc* 24:243–247
- Tindall JA, Kunkel JR (1999) *Unsaturated zone hydrology for scientists and engineers*. Prentice-Hall, Englewood Cliffs, p 624
- van Genuchten MT (1980) A closed-form equation for predicting the hydraulic conductivity of unsaturated soils. *Soil Sci Soc Am J* 44(5):892–898
- Wang D (2002) Dynamics of soil water and temperature in aboveground sand cultures used for screening plant salt tolerance. *Soil Sci Soc Am J* 66(5):1484–1491
- Yamanaka T, Yonetani T (1999) Dynamics of the evaporation zone in dry sandy soils. *J Hydrol* 217(1–2):135–148
- Zhang T, Berndtsson R (1991) Analysis of soil–water dynamics in time and space by use of pattern-recognition. *Water Resour Res* 27(7):1623–1636
- Zhao Y, Paul W, Yiming W (2002) Comparison of soil water content measurements with SWR-, FD- and TDR sensors. *Z Be-wässerungswirtschaft* 37(1):17–31